Structure and dynamics of the $4p \rightarrow ns,md$ autoionizing resonances between the ^3P and ^1S thresholds in atomic bromine

S. Benzaid, M. O. Krause, A. Menzel,* and C. D. Caldwell
Department of Physics, University of Central Florida, Orlando, Florida 32816-2385
(Received 22 December 1997)

The relative partial photoionization cross sections σ_i and photoelectron angular distribution parameters β_i are measured for all possible final ionic states of Br^+ between the $^3P_2$ and $^1S_0$ thresholds. The decay patterns of the autoionizing $4p^4\,{}^3P_{1,0}\,n\ell$, $4p^4\,{}^1D_2\,n\ell$, and $4p^4\,{}^1S_0\,n\ell$ Rydberg series arising from the $4p \rightarrow ns,md$ excitations are observed at the fine-structure level in all available channels. For each Rydberg series, the energies, quantum defects, and photoelectron angular distribution parameters are determined, as well as the widths and shape parameters of the low-lying members. Relative total cross sections are derived from the partial cross sections and from ion-yield measurements over the lowest members of the $^3P_{1,0}$ and $^1D_2$ series. All major spectroscopic and dynamic properties of these series are reported for this open-shell atom. Conclusions are drawn from the comprehensive data sets in comparison with other halogen atoms and the neighboring closed-shell rare gas atoms. Our results, encompassing the entire autoionization regime, are compared with other experimental data and theoretical calculations, where available. [S1050-2947(98)06106-X]

PACS number(s): 32.80.Fb, 32.80.Hd

I. INTRODUCTION

In analogy to the Beutler-Fano autoionizing resonances between the fine-structure components of the rare gases, autoionizing resonances occur between the multiplet components of the halogen atoms. Delineation of these resonances is of importance because (a) the halogen atoms, with their p^5 configuration, are a first stepping stone from the closed-shell structure of the rare gases to the more complex structure of open-shell atoms and (b) the halogen atoms, being radicals, play significant roles in chemistry and in the upper atmosphere. We report here on a comprehensive study of the properties of the $4s^24p^4(^3P_{1,0},^1D_2,^1S_0)ns,md$ resonances arising from $4p \rightarrow n\ell$ photoexcitation of the bromine atom, Br $4s^24p^5(^2P_{3/2})$. Analysis of the electrons associated uniquely with the final ionic states Br^+ $4s^24p^4(^3P_2,^3P_1,^3P_0,^1D_2)$ created in the decay of the resonances allowed us to examine the important aspects of the electronic structure and dynamics, ranging from the energies and quantum defects to the (relative) partial cross sections and electron angular distributions for the resonances of all Rydberg series.

Presumably due to complexities facing theory for a mid-Z element with an open-shell configuration, and strong chemical reactivity facing experiment, photoexcitation and photoionization studies of Br have received rather scant attention thus far. On the theoretical side, photoionization studies are limited to a few reports [1–5], and only Robicheaux and Greene treated the autoionization regimes [4,5]. On the experimental side, work since the compilation by Moore [6] comprises studies by photoabsorption [7,8], photoemission [9,10], ion yield [11], He I photoelectron spectrometry [12–15], multiphoton ionization [16], and, most recently, electron emission [17,18]. Among the most relevant works in the present context are the spectroscopic studies by Sarma and Joshi [8], who measured all series except the $^1S_0$ series, and by Martin and Tech [9,10], who determined, *inter alia*, the series limits, the ion-yield measurement by Ruščić *et al.*, whose data include the total cross section, but only one ns,md pair of the $^1S_0$ series, and the theoretical treatment by Robicheaux and Greene [4], who present the variation in the *total* cross section across the resonances of all series.

An important result of our investigation has recently been presented [18]; it concerns the observation of a spin-orbit-induced autoionization pathway in the $(^1D_2)ns,md$ series. In the following, we summarize the results of our comprehensive study of the entire autoionization regime extending from the first ionization threshold, Br^+ $4p^4(^3P_2)$, to the highest threshold, Br^+ $4p^4(^1S_0)$, of the multiplet created by the ionization of a $4p$ electron.

II. GENERAL BACKGROUND

Ionization of the $4p$ subshell of atomic bromine creates a five-component multiplet of the bromine ion. The energies of the multiplet levels are well known [7,9,10] and are listed in Table I for convenience. If the excitation energy covers the

TABLE I. Energy levels (ionization thresholds) of Br^+ $4s^24p^4$.

State	E (eV) [a]
$^3P_2^e$	11.8138
$^3P_1^e$	12.2027
$^3P_0^e$	12.2896
$^1D_2^e$	13.3127
$^1S_0^e$	15.2689

[a]From Refs. [9,10], using the conversion factor 1239.8424 nm eV; uncertainties are ≤ 0.1 meV.

*Present address: Department of Molecular Interactions, Max-Planck-Institut für Strömungsforschung, Bunsenstrasse 10, D-37073 Göttingen, Germany.

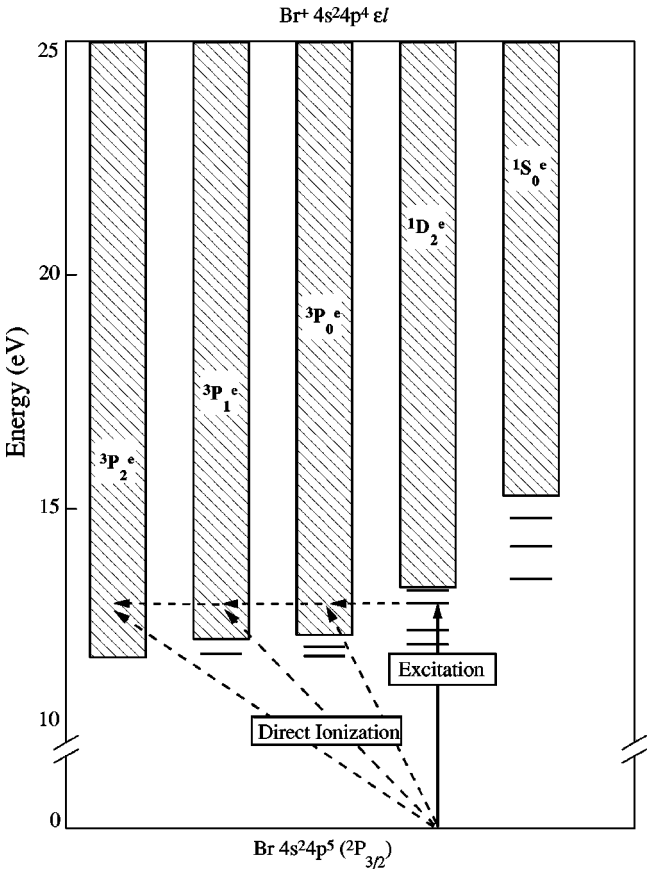

FIG. 1. Energy diagram of atomic bromine showing the Br^+ $4p^4(LSJ)$ continua and the excitation of a $4p$ electron to an autoionizing state, together with the available ionization pathways.

interval given by the multiplet splitting, $E(^3P_2)=11.81$ eV to $E(^1S_0)=15.27$ eV, ionization proceeds directly or indirectly via the autoionizing Rydberg resonances converging to the various ionization thresholds. The two coherent pathways are sketched in Fig. 1 and are given as follows:

$$\begin{array}{ccc} & & Br^* \; 4s^2 4p^4(^3P_1^e,\ ^3P_0^e,\ ^1D_2^e,\ ^1S_0^e)\ \ ns,md \\ & \nearrow & \\ Br\ 4s^2 4p^5(^2P_{3/2}) & & \downarrow \\ & \searrow & \\ & & Br^+\ 4s^2 4p^4(^3P_2^e,\ ^3P_1^e,\ ^3P_0^e,\ ^1D_2^e,\ ^1S_0^e) + \epsilon s, \epsilon d \end{array} \tag{1}$$

where the final state will couple in the LS scheme to $^2S,^2P,^2D,^2F,^4P,^4D,^4F$. Table II summarizes the coupling possibilities which are significant in our work. As indicated in Eq. (1), we are concerned only with excitation from the $^2P_{3/2}$ ground state, because the excited $^2P_{1/2}$ state, which lies 0.4569 eV above the ground state, makes no contribution.

In the Rydberg formula

$$E_n = E_\infty - \frac{\mathcal{R}(\mathrm{Br})}{(n\ -\mu)^2} \tag{2}$$

TABLE II. Optically allowed Rydberg series and the continua into which they can decay in the LS notation.

Series	Continua
$4s^2 4p^4(^3P_0)ns\ ^2P$	$^3P_2\ \epsilon s/\epsilon d$
$md\ ^2D$	$^3P_2\ \epsilon d$
$4s^2 4p^4(^3P_1)ns\ ^2P$	$^3P_2\ \epsilon s/\epsilon d$
$md\ ^2P$	$^3P_2\ \epsilon s/\epsilon d$
$4s^2 4p^4(^1D_2)\ ns\ ^2D$	$^3P\ \epsilon d$
$md\ ^2P$	$^3P\ \epsilon d/\epsilon s$
$md\ ^2D$	$^3P\ \epsilon d$
$md\ ^2S$	$^3P_2\ \epsilon d$ [a]
$md\ ^2F$ [b]	$^3P\ \epsilon d$
$4s^2 4p^4(^1S_0)\ ns\ ^2S$	$^1D\ \epsilon d$
$md\ ^2D$	$^3P\ \epsilon d,\ ^1D\ \epsilon d/\epsilon s$

[a]Decay possible through spin-orbit interactions.
[b]Excitation possible through spin-orbit interactions.

a constant of $\mathcal{R}(\mathrm{Br})=13.605\,604$ eV applies. The limits E_∞ are equivalent to the energy levels listed in Table I, and μ is the quantum defect. The energies are the *resonance* energies E_n of the autoionization profiles; they differ from the *peak* energies E_m according to $E_m=E_n+\Gamma/2q$, where Γ is the width and q the shape parameter of the resonance profile [19]. Resonance energies are obtained from Shore fits [20,21]:

$$\sigma_i = c_i + \frac{a_i\epsilon + b_i}{1+\epsilon^2}, \tag{3}$$

which are applied to the experimental total cross sections as well as to the measured partial and differential cross sections with the bandpass folded into the function [19,22]. The parameters a_i and b_i refer to the shape of the resonance and can be converted to the parameter given in the Fano formulation [23] as q_i, while ϵ is the reduced energy in terms of the resonance widths Γ. The ''background'' cross section is given by c_i, which is the sum of the interacting (σ_a) and non interacting (σ_b) parts of the cross section, $c_i=\sigma_a+\sigma_b$, as introduced in the Fano model [23]. In our analysis, the bandpass is removed following the fit of the data and the ''true'' parameters are thus obtained. However, these resonance parameters should not be viewed as equivalent to those defined by Fano and Shore, because the condition of an *isolated* resonance [20,21,23] is generally not fulfilled in the present work. Instead the parameters obtained by using Eq. (3) as a mathematical tool will be presented for heuristic purposes in the discussion of those series members that are subject to various interactions.

In addition to the determination of the energies, widths, and shape parameters of the resonances, relative intensities are determined for the members of the series based on $^3P_{1,0}$. Using the values for the widths Γ, the cross section σ_a and the shape parameter q resulting from the fits of the resonance profiles we determined I from

$$I \propto \sigma_a \Gamma (q^2-1), \tag{4}$$

which gives a quantity that is proportional to the excess oscillator strength [21] with σ_b set to zero.

III. EXPERIMENTAL SETUP AND PROCEDURES

The experiment was performed at the University of Wisconsin Synchrotron Radiation Center (SRC). The ionizing radiation was provided by a bending magnet in conjunction with a 4 m normal incidence monochromator (NIM) equipped with a 1200 lines/mm gold-coated MgF_2 grating. Our electron spectrometer, the atomic source, and experimental procedures have been described elsewhere [17,19,24–26]. Pertinent details are given in the following.

Using two out of three analyzers mounted at right angles to each other on a rotatable platform perpendicular to the direction of the photon beam, we measured either the relative partial cross section σ_i or the photoelectron angular distribution parameter β_i for decay into channel i according to

$$I(\theta)_i \propto \frac{d\sigma_i}{d\Omega} = \frac{\sigma_i}{4\pi}\left(1+\frac{\beta_i}{4}(1+3p\,\cos 2\theta)\right). \tag{5}$$

For measurements of σ_i the angle θ, which is measured with respect to the major polarization vector, is set to the ''magic'' angle $\theta_m=(1/2)\cos^{-1}(-1/3p)$ for which the term proportional to β_i vanishes. For a measurement of β_i the angles $\theta=0°$ and 90° are used, from which

$$\beta_i=\frac{4(R_i-1)}{3p(R_i+1)-(R_i-1)}, \tag{6}$$

where R_i is the ratio of $d\sigma_i/d\Omega$ at 0° to $d\sigma_i/d\Omega$ at 90° and p is the polarization of the photon beam, which we determined to be $p=0.85(1)$. The analyzers were set to a resolution of typically 50 meV (full width half maximum, FWHM), sufficient to separate all the multiplet components (cf. Table I). Two modes of operation are used, the photoelectron spectrometry (PES) mode and the constant ionic state (CIS) mode. As described in various places [17,18,24,26,27], the CIS spectra dependably reveal the resonance structures in both σ_i and β_i for each of the channels i, at a resolution given by the bandpass of the photon beam, while PES recordings at suitably chosen photon energies relate the partial cross sections σ_i to one another and calibrate the β_i CIS spectra. The three-dimensional (3D) plot of Fig. 2 illustrates the two modes and their relationship by way of CIS spectra for the $^3P_2$ and $^1D_2$ ionic states in several regions of the autoionizing Rydberg series and a PES plot at $h\nu=16$ eV.

In this work the energy calibration of the monochromator is a major concern. We relied on the narrow Xe $5p_{1/2}ns'$, $n=10-16$, and the Kr $4p_{1/2}ns'$, $n=9-11$, resonance lines with their accurately known energies (within 0.03 meV) [28,29]. The resulting calibration curve, basically linear in λ, provided a reference with an accuracy of ± 0.7 meV between 11.8 and 14.5 eV. The monochromator bandpass was determined by reference to the narrow resonance lines, Xe $5p_{1/2}$,$13s'$ and $14s'$ and Ar $3p_{1/2}15s'$, and the so-called zero-order scans, which also yielded the beam contour. For a typical setting of 60 μm for entrance and exit slits, the bandpass was found to be 16.0(8) pm (FWHM), or 1.8 meV at 12 eV. The contour is essentially Gaussian.

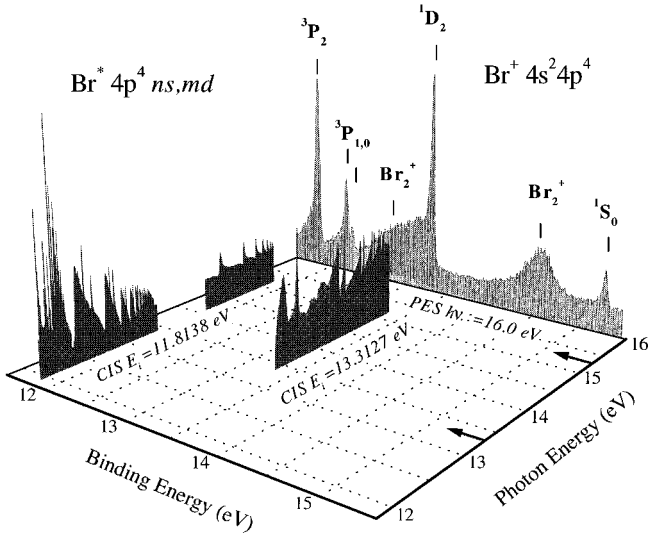

FIG. 2. 3D plot of ionization in the $4p\rightarrow n\ell$ autoionization regime of Br as seen by electron spectrometry in the PES and CIS modes of operation. The arrows indicate the $^1D_2$ and $^1S_0$ ionization thresholds.

Bromine atoms were produced by dissociation of Br_2, purity 99.99%, in a 2.45 GHz microwave discharge as described previously [17]. Only about 14 W were dissipated in the air-cooled tube to optimize stability and to minimize the noise level. The discharge tube was thinly coated with phosphorous pentoxide and the flow tube, which guided the atoms to the source cell, was thinly coated with halocarbon wax. An atom yield of about 70% was measured in the source cell at a distance of 30 cm from the discharge. No direct line of sight existed between the source cell and the discharge tube. It is to be noted that no discharge products, such as HBr and excited Br, could be discerned in the PES spectra, as may be judged from Fig. 1 of Ref. [18].

All spectra were corrected for background contributions, normalized to the photon flux according to the current from a nickel mesh located after the monochromator exit slit, and adjusted to the response of the electron analyzers and detection system. PES scans at the beginning and end of a CIS scan, which may last up to 60 minutes, safeguarded against unrecognized drifts in target density and surface potentials along the electron paths. Tests for spurious signals from molecular bromine proved negative in CIS runs on pure Br_2, except in the position of the $Br^+(^1D_2)$ state, which overlaps with the $Br_2^+(^2\Pi_u)$ band.

To complement the electron spectra, total ion yields were measured for a few resonance groups, with emphasis on regions just above the ionization thresholds, where the low-energy electrons are difficult to detect. Ions were allowed to drift through the apertures of the source cell [25] at their thermal energies before being accelerated into the analyzer, used as a velocity filter, and then impinging on the detector at a total energy of 2.5 keV. Obviously, only the photon energy needed to be changed to record an ion spectrum, but without mass analysis Br_2^+ ions give rise to a considerable

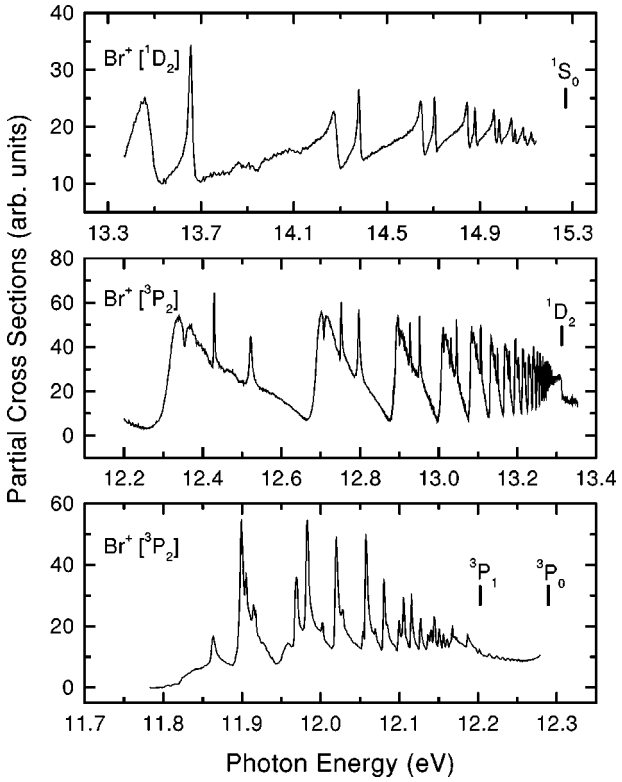

FIG. 3. Overview of the autoionization series converging to the $^3P_{1,0}$, $^1D_2$, and $^1S_0$ limits. The electron spectra are recorded at the magic angle in the partial channels indicated [$Br^+(^3P_2)$ or $Br^+(^1D_2)$]. Relative cross sections are approximate.

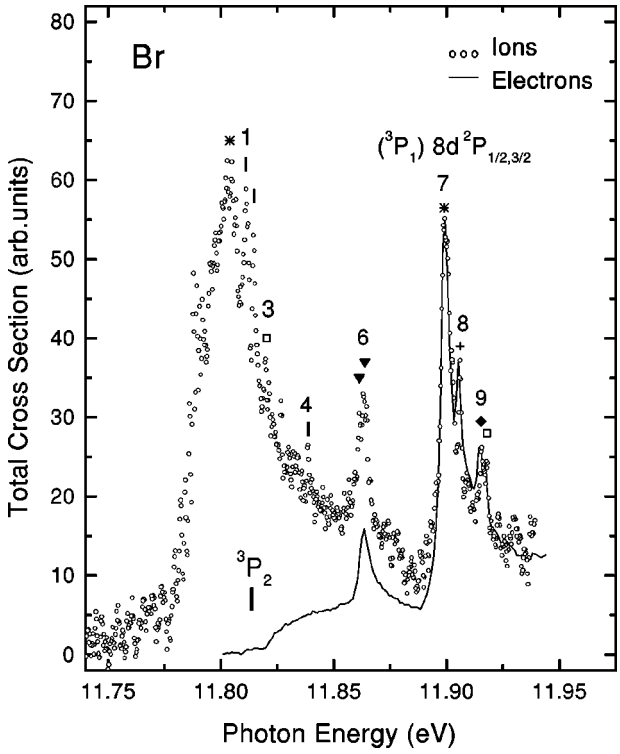

FIG. 4. Autoionization structure of the Br $4p^4(^3P_{1,0})ns,md$ series near the $^3P_2$ ionization threshold, as seen in electron emission and ion-yield measurements. The two spectra are matched at peak no. 7. The bandpass is 16 pm (FWHM) for the electrons and 8 pm for the ions. The symbols are explained in Fig. 5.

background. This generally smooth background could be subtracted to a good approximation with the aid of an ion-yield spectrum from Br_2 alone.

IV. RESULTS AND DISCUSSION

A. Overview

The resonance series based on the $^3P_{1,0}$, $^1D_2$, and $^1S_0$ thresholds are shown in Fig. 3. The spectra represent long-range CIS scans at moderate resolution, with the first members of the series added on from separate runs. The $^3P_{1,0}$ series is recorded in the $^3P_2$ $\epsilon\ell$ channel and represents the total cross section $\sigma_{\rm tot}$ up to the $^3P_1$ threshold; the $^1D_2$ series is also recorded in the $^3P_2$ $\epsilon\ell$ channel and represents the partial cross section $\sigma(^3P_2)$, which pertains to the dominant decay mode; and the $^1S_0$ series is recorded in the strong $^1D_2$ $\epsilon\ell$ channel. Each of the spectra has been corrected and normalized as described in Sec. III, but the cross section scales of the three panels are interrelated only approximately, as no special effort was expended to determine the cross section over the entire range of autoionization and beyond. All partial and total cross sections reported in our work are relative cross sections. We note that a previous experiment [11] and theory [4] report $\sigma_{\rm tot} \approx 90$ Mb at 12.34 eV at the maximum of the broad $(^1D_2)5d\ ^2P,^2D$ resonance.

B. The $(^3P_{1,0})ns,md$ series

Of the 12 allowed series converging to the $^3P_1$ threshold and the five series converging to the $^3P_0$ threshold [8,9], only two series of each are clearly developed in the autoionization regime in the case of photoexcitation, and an additional series can be discerned. However, none of these form regular intensity patterns. This observation must be attributed to interchannel coupling between series, involving also members of the $(^1D_2)$ $6s,4d$ group, most of which have been observed in the discrete spectrum just below the $^3P_2$ threshold [9]. The $^3P_{1,0}$ series are presented as $\sigma(^3P_2)$ in Figs. 3–6 and also as $\beta(^3P_2)$ in in Figs. 5 and 6. The data for both σ and β are internally self-consistent because both are derived from the same differential cross sections measured at 0° and 90°. A direct determination of σ was also made at the angle θ_m; both sets of σ data agree excellently with each other. The electron CIS spectrum of Fig. 4 is supplemented by an ion-yield spectrum because of the fading transmission for low kinetic energy electrons, $E_{\rm kin} \leqslant 70$ meV, through the electron-optical components. Due to the thermal energies of the ions, about 25 meV, the spectrum extends below the first ionization threshold. The various features in the figures are labeled in consecutive order and marked by symbols corresponding to the identifiable series. Energies, quantum defects, resonance widths, and shape parameters are summarized in Tables III and IV. As done in previous work [8,11], we used the quantum defect μ to make series assignments. The β and q parameters measured in our work provided additional criteria. Nevertheless, ambiguities persist in a few cases. For example, a value of $\mu = 1.39$ for $(^3P_1)11d$ fits better into the series if assigned to peak 18 than does $\mu = 1.27$ if assigned to peak 19, whereas a value of $q = 5.4$ for peak 18 is not as good as $q = 3.0$ for peak 19. A reassign-

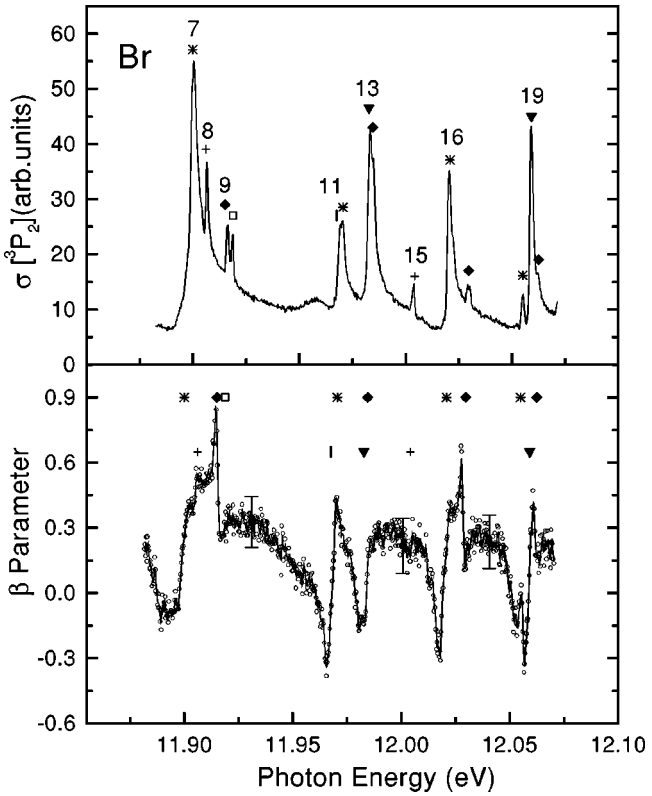

FIG. 5. Autoionization structure of the Br $4p^4(^3P_{1,0})ns,md$ series. Both σ_i and β_i are derived from CIS scans of the differential cross sections at 0° and 90° for the $Br^+(^3P_2)$ ionic state. Note that σ_i is equivalent to σ_{tot} up to the $^3P_1$ limit. The σ_i scale is matched with those of Figs. 3, 4, and 6. Points with error bars are from PES measurements. Symbols denote the various series: $(*)(^3P_1)md\ ^2P_{3/2,1/2}$; $(\blacktriangledown)(^3P_0)md\ ^2D_{3/2,5/2}$; $(\blacklozenge)(^3P_1)ns^2P_{3/2}$; $(+)(^3P_0)ns\ ^2P_{1/2}$; $(\square)(^3P_1)ns\ ^4P$. Tick-marks indicate unidentified resonances. Lines through the β data correspond to a three-point smoothing and are intended to guide the eye. The bandpass is 1.8 meV and the step size 0.4 meV.

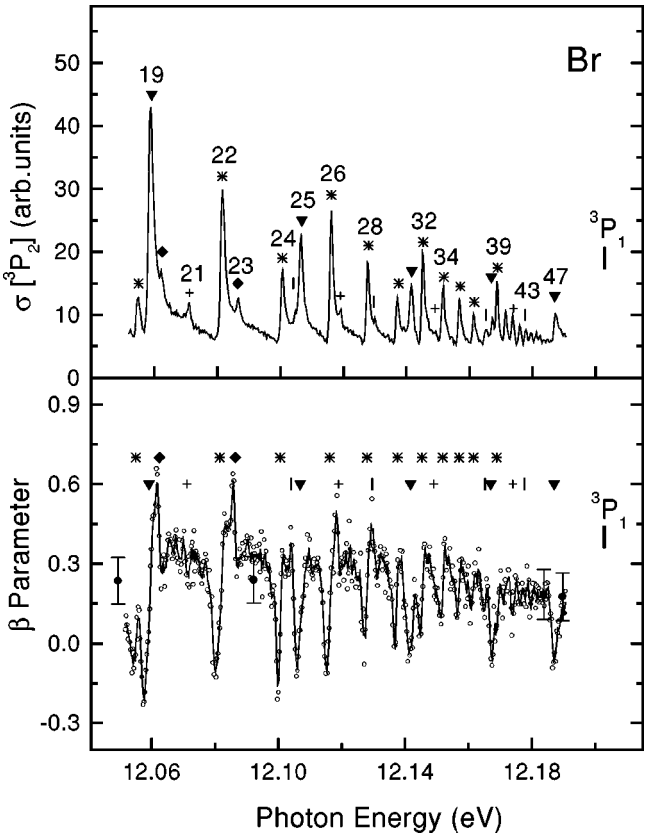

FIG. 6. Autoionization structure for the higher members of the Br $4p^4(^3P_{1,0})ns,md$ series. Explanations are the same as for Fig. 5.

ment, which we do not favor, would leave peak 18 unidentified and make $(^3P_1)11d$ coincident with $(^3P_0)9d$ (see Table III).

At a photon bandpass of 8 pm, or 0.9 meV, many more resonances are observed than in previous work [8,11]. Shore profiles, Eq. (3), equivalent to Fano profiles, can be fitted to allow one to determine the resonance energy. Our energies given in the tables have an uncertainty of ± 2 meV, which combines all uncertainties inherent in the energy determination. Previously reported energies are in good accord with our values, but are greater by 2 to 3 meV on the average. The quantum defects are $\mu \approx 1.39$ for the md levels and $\mu \approx 3.11$ for ns levels, with little difference between the $^3P_1$ and $^3P_0$ series. Within the error limits, the μ values are rather constant, except for $(^3P_1)md\ ^2P$, where μ is increasing. A value of $\mu \approx 3.06$ applies to the $(^3P_1)ns\ ^4P_{1/2}$ series in Table IV, which is identifiable in our spectrum on the basis of the antecedents below the $^3P_2$ threshold [9] and the $9s$ member reported at 11.820 eV [8] and seen in Fig. 4 at 11.820 (2) eV (peak 3). Fine-structure splitting occurs in several series. However, only the splittings of $(^3P_1)7d\ ^2P_{3/2,1/2}$ and $(^3P_0)7d\ ^2D_{5/2,3/2}$ are resolved. The ^2P doublet is seen in Fig. 4 at 11.803 and 11.805 eV just below the $^3P_2$ threshold, and the splitting of 1.9 (3) meV is roughly compatible with the splitting of members in the discrete part of the spectrum [9]. Similarly, the splitting of the ^2D doublet, observed by us, is compatible with the data in the discrete spectrum [8,9]. The positions of the double peak components, nos. 11,12 and nos. 13,14, were pinpointed in a scan at a bandpass of 4 pm (0.5 meV).

Many resonances are broader than the bandpass, be it due to the lifetime of the excitation states or a closely spaced doublet or both. All md members are broad and have a pronounced tail toward the higher energies, as is common for autoionizing d states in other series of the halogens, the rare gases, and other elements [30], with the exception of the atoms in the first row. By contrast, but in accord with expectations, the ns members are sharp and appear symmetric. The region up to $h\nu = 12.15$ eV was fit by a Shore profile, folded with the applicable bandpass [19]. The Fano q parameters are calculated from the Shore parameters following removal of the bandpass function and are listed, together with the resonance widths Γ, in Table III. It must be remembered that in some instances the width may be an effective width for an unresolved, or unresolvable, doublet. For the md series, we estimate the resonance widths for the doublet components to be up to 20% smaller than the Γ values obtained from the fits and listed in Table III. The uncertainties in Γ, and also in q, are derived from the fitting procedure and do not include the influence of the doublet structure.

Finally, the energies of the resonances between $^3P_1$ and $^3P_0$ (see Fig. 3) are included in Table V. The profiles, as seen in the $Br^+(^3P_2)\epsilon\ell$ channel, recommend their assign-

TABLE III. The $(^3P_{1,0})ns,md$ series: Energies E, quantum defects μ, intensities I, shape parameters q, and widths Γ.

			ΔE (meV) [c]					
Label [a]	Member	E (eV) [b]	Ref. [11]	Ref. [8]	μ	I [d]	q	Γ (meV)
8	$(^3P_0)9s$	11.906	−2	−3	3.04(1)	40	2.1	1.5
15	$(^3P_0)10s$	12.004	0	+3	3.09(2)	17	−5.9	1.1
21	$(^3P_0)11s$	12.071	+1	+2	3.11(3)			
27	$(^3P_0)12s$	12.119	−1	−1	3.06(5)			
33	$(^3P_0)13s$	12.149		+6	3.15(6)			
5	$(^3P_0)7d$	11.861	+5	+6	1.359(2)	110	4	5
6		11.864				60	5.9	3
13	$(^3P_0)8d$	11.983	+2	+4	1.34(2)	248	4.3(2.0)	3.1(3)
19	$(^3P_0)9d$	12.059	+3	+3	1.32(3)	126	3.0(1)	1.6(1)
25	$(^3P_0)10d$	12.107	+2	+2	1.37(4)	47	2.8(5)	1.2(1)
31	$(^3P_0)11d$	12.142	+2	+2	1.40(6)	42	9.1(1.8)	1.4(1)
38	$(^3P_0)12d$	12.167	0	+2	1.44(8)			
47	$(^3P_0)13d$	12.187			1.4(1)			
9	$(^3P_1)10s$	11.919	−1	+1	3.08(2)	21	−6.9	0.7
14	$(^3P_1)11s$	11.984	+1	+3	3.10(3)	17	−1	0.6
17	$(^3P_1)12s$	12.030			3.13(4)			
20	$(^3P_1)13s$	12.062			3.15(6)			
23	$(^3P_1)14s$	12.086			3.18(8)			
	$(^3P_1)7d$	11.803			1.15(2)			
		11.805						
7	$(^3P_1)8d$	11.900	+4	+3	1.29(2)	554	4.8(8)	5.2(1)
12	$(^3P_1)9d$	11.970	+4	+4	1.34(3)	162	2.5(5)	3.0(3)
16	$(^3P_1)10d$	12.021	+1	+2	1.35(4)	158	3.2(1)	2.3(1)
18	$(^3P_1)11d$	12.055	+7	+2	1.39(6)	28	5.4(1)	1.7(1)
22	$(^3P_1)12d$	12.081	+4	+3	1.43(8)	68	2.9(1)	1.2(1)
24	$(^3P_1)13d$	12.101		+2	1.4(1)	32	2.5(1)	1.2(1)
26	$(^3P_1)14d$	12.116		+2	1.4(1)	66	3.4(1)	1.0(1)
28	$(^3P_1)15d$	12.128		+2	1.5(2)	24	2.3(1)	0.8(2)
30	$(^3P_1)16d$	12.137		+2	1.5(2)	21	2.7(1)	0.8(2)
32	$(^3P_1)17d$	12.145		+3	1.6(2)	11	1.5	0.8
34	$(^3P_1)18d$	12.152		+3	1.6(3)			
35	$(^3P_1)19d$	12.157			1.7(3)			
36	$(^3P_1)20d$	12.161			1.8(4)			
39	$(^3P_1)21d$	12.165			1.9(5)			

[a]The labels refer to Figs. 4–6.
[b]Uncertainty is ±2 meV.
[c]Referred to our energy E.
[d]Arbitrary units.

TABLE IV. The $(^3P_1)ns\ ^4P_{1/2}$ series.

Label	Member	Energy (eV)		μ
		This work	Ref. [8]	
	$(^3P_1)7s$		11.326	3.062
	$(^3P_1)8s$		11.652	3.030
3	$(^3P_1)9s$	11.820	11.820	3.03(2)
10	$(^3P_1)10s$	11.919		3.08(2)

ment to the presumably dominant $(^3P_0)md\ ^2D$ series. Because of the weak signal in this region, we report for the energies the *peak* values of the resonance profiles. No attempt was made to investigate this region in the $(^3P_1)\epsilon\ell$ channel or by an ion-yield scan.

One striking feature of the spectra in Figs. 4–6 is that the intensities for a given series do not follow regular patterns. As pointed out above, interchannel coupling is the most likely reason for this. Coupling with other members of the $^3P_{1,0}$ series and with members of the $(^1D)ns,md(^2P,^2D,^2S,^2F)$ group is possible. Surprisingly, this coupling seems to affect some members of the series more strongly than others, while at the same time no corre-

TABLE V. Energies and assignment of resonances between the $^3P_1$ and $^3P_0$ limits.

Member	Energy (eV) [a]	μ
$(^3P_0)14d$	12.206	1.2(1)
$(^3P_0)15d$	12.217	1.2(2)
$(^3P_0)16d$	12.227	1.2(2)
$(^3P_0)17d$	12.236	1.0(3)
$(^3P_0)18d$	12.242	1.0(3)
$(^3P_0)19d$	12.248	0.9(4)
$(^3P_0)20d$	12.252	0.9(5)
$(^3P_0)21d$	12.256	0.9(6)
33333		

[a]Peak energy, uncertainty ± 3 meV.

lations can be made for μ, which behaves rather regularly. The intensities are calculated with the aid of Eq. (4) and given in Table III.

An overall visual comparison of our spectrum, shown in the lower panel of Fig. 3, with the experimental results of Ref. [11] and the theoretical results of Ref. [4] indicates some variance with the data of Ruščić, Greene, and Berkowitz [11] and a satisfactory overall accord with the calculations by Robicheaux and Greene [4].

The angular distribution parameters β reveal an average value of $\beta \approx 0.3$ across the series, with excursions to $\beta = 0.9$ and $\beta = -0.3$ at the resonances. As seen in Figs. 5 and 6, β_i for each md resonance is preceded by a negative dip and followed past the maximum by a slow decline toward higher energies. This behavior is reminiscent of the behavior of d resonances in the outer shell of the rare gases Ar to Xe [22,31] and in Cl [32], and it repeats in the other series of Br (see below). The analogy applies also to the s resonances, which produce slight dips here and in all the above instances. Generally, the excursions in β are dampened by comparison with the rare gases due to the greater number of exit channels accessible and the increased coupling possibilities in an open-shell atom.

In concluding this section, attention is drawn to the fact that the various resonance parameters, especially q, Γ, and I, are not those applicable to isolated resonances. The deviations from the patterns of a noninteracting series are especially evident in the shape parameters and the intensities and, to a lesser extent, the widths of the resonances. However, the deviations are not solely due to the effects of interactions with perturbers, but also due to the presence of an unresolved doublet structure for most series members. There is probably little hope that even a much higher resolution than used in this work could decisively separate the components.

C. The $(^1D_2)ns,md$ series

This series is presented in its entirety in Fig. 3. Shown is the partial cross section $\sigma(^3P_2)$, which displays all salient features seen also in the total cross section. This becomes apparent by a comparison of $\sigma(^3P_2)$ with $\sigma_{\rm tot}$, recorded directly by an ion-yield measurement for the first and second groups of the series ($7s,5d$, and $8s,6d$ members) and $\sigma_{\rm tot}$, formed as the sum of all partial cross sections σ_i as done for the second and third groups.

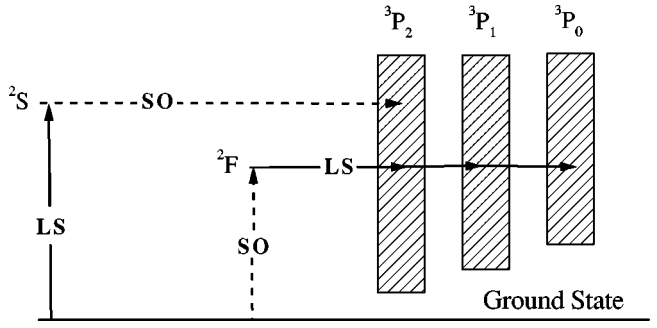

FIG. 7. Schematic diagram showing how the ^3P continua are reached via the ^2S and ^2F excited states. Spin-orbit-induced transitions are denoted by SO and LS-allowed transitions by LS.

Previously we reported the most significant results for the $^1D_2$ series: the observation of the LS-forbidden ^2F resonance series and the partition of $\sigma_{\rm tot}$ into σ_i of all available ionization channels i [18]. Here, we supplement the σ_i data by the β_i results and report on other properties of the series. The series that can be populated by the excitation of a $4p$ electron are summarized in Table II, where we denote the two series that require spin-orbit interactions to couple to the continua. Figure 7 illustrates the difference for these two series: Excitation of ^2S from the $^2P_{3/2}$ ground state is LS allowed, but requires spin-orbit interaction to decay into the $^3P_2$ continuum via coupling of the $^1D_2$ and $^3P_2$ core states; excitation of ^2F can proceed only by spin-orbit coupling, but the ^2F is LS allowed to decay into all three $^3P_{2,1,0}$ continua [4,18].

In Fig. 8, the σ_i for the $8s,6d$ group are juxtaposed to the β_i values for the same decay channels i: $Br^+(^3P_2)\epsilon\ell$, $Br^+(^3P_1)\epsilon\ell$, and $Br^+(^3P_0)\epsilon\ell$. The data presented for σ_i and β_i have a common source, namely, the differential cross sections $d\sigma/d\Omega$ at 0° and 90°. The $d\sigma/d\Omega$ CIS spectra are fitted by a Shore function [20] convoluted with our bandpass (8 pm or 1 meV). The fit curves are then substituted into Eqs. (5) and (6) to calculate the (relative) σ_i displayed in Fig. 8 and the β_i, represented as solid lines in the figure. The resulting β_i (or σ_i) curves constitute a natural fit to the β_i (or σ_i) calculated using individual data points. Also shown in the figure are the individual data points for β_i. This procedure dispenses with any additional parameters that would be required for a *direct fit* of the β data [33]. Another advantage of our method lies in the capability of removing the bandpass contribution and thus to calculate the ''true'' β_i values. For the very narrow resonance $8s\ ^2D$ the minimum β value then becomes $\beta(\text{true}) = 0.16$ for $^3P_0$ rather than $\beta(\text{conv}) = 0.30$. Excursions in β_i for the other resonances are hardly modified because the resonance widths are considerably larger than the bandpass. Regarding the partial cross sections, we find σ_i derived from $d\sigma/d\Omega$ to be in good overall agreement with σ_i measured directly at θ_m (cf. Ref. [18]).

As has already been pointed out in Sec. IV B, the md resonances are broad and the ns resonances are narrow, thus following a general pattern. The LS-forbidden $md\ ^2S$ and $md\ ^2F$ resonances are exceptions. They are rather narrow but somewhat broader than $ns\ ^2D$. Similarly, the general behavior of β_i fits the general trend discussed above in context with the $(^3P_{1,0})ns,md$ series. However, distinctive differences appear in the three partial channels. For $\beta(md\ ^2F)$,

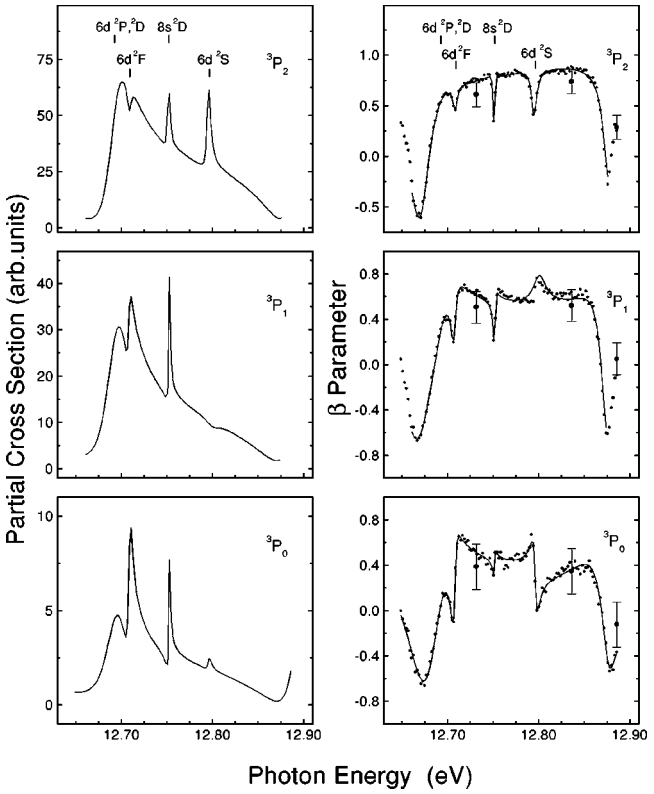

FIG. 8. Partial cross sections σ_i and β_i parameters for the $Br^+(^3P_{2,1,0})$ components across the $(^1D_2)8s,6d$ resonances. Solid points are data points, and all solid lines are calculated from convoluted Shore fits of the differential cross sections at 0° and 90°. Points with error bars are PES data. Scales for σ_i are in the proper ratios, as determined by PES recordings. The bandpass is 2.0 meV and the step size is 2 meV.

the dispersive shape becomes increasingly pronounced in going from decay into $^3P_2$ to $^3P_1$ to $^3P_0$. For $\beta(ns\ ^2D)$ the excursion is windowlike in $^3P_2$, as it is for Kr [22], but dispersionlike in $^3P_1$ and $^3P_0$. For $\beta(md\ ^2P,^2D)$ the behavior is similar in all channels, with β_i for $^3P_2$ being higher than for $^3P_{1,0}$. The minimum value for this series is $\beta_{\min} \approx -0.7$, which is greater than $\beta_{\min} \approx -1$ in the case of Kr [22]. This difference is presumably due to the overlap of two series in Br, thus providing more $\epsilon\ell$ channels and hence a less sharply defined minimum.

The β_i spectra confirm the spin-orbit-induced decay of $md\ ^2S$ into $^3P_2\ \epsilon\ell$ and the weak indication in σ_i for the decay into $^3P_0\ \epsilon\ell$. The latter decay must be mediated via the $^1S_0$ core which would couple sufficiently strongly with the $^3P_0$ core in spite of the large energy separation between the two core states. A slight excursion in β_i is also observed in $^3P_1\ \epsilon\ell$. An interpretation seems to require an interaction with the $^3P_1$ series to be invoked, since a signal arising from the tails of the $^3P_2$ and $^3P_0$ components can be excluded by the incompatible shapes of the excursions.

The differences in σ_i for the various channels may be expressed in the shape parameter q_i. These parameters were obtained from a fit to two sets of data for the $8s,6d$ group and are listed in Table VI. As expected from Fig. 8, q_i displays the greatest variation for $6d\ ^2F$.

Resonance energies and quantum defects for members of all $^1D_2$ series are listed in Table VII. The quantum defects

TABLE VI. Shape parameters q_i for the $(^1D_2)8s,6d$ group in the ^3P_J channels.

Resonance	$^3P_2$	$^3P_1$	$^3P_0$	Total
$6d\ ^2PD$	1.8(2)	2.2(1)	2.6(2)	1.9(2)
$6d\ ^2F$	0.4(3)	0.9(1)	1.6(1)	0.7(2)
$6d\ ^2S$	6.7(4)			7.2(3)
$8s\ ^2D$	4.9(4)	3.8(3)	2.7(1)	5.5(5)

are seen to be constant for each series. While $\mu \approx 3.07$ for the $(^1D_2)ns$ series is virtually identical with the μ for the corresponding $^3P_{1,0}$ series members as is $\mu \approx 1.32$ for the LS-allowed $(^1D_2)md$ series, the LS-forbidden ^2F series has a slightly lower value of $\mu \approx 1.25$ and the LS-forbidden ^2S series has a much lower value, $\mu \approx 0.87$. The energies from previous work [8,11] agree satisfactorily with our values for the ns series, but show a greater variance for the md series, especially in the case of the energies [34] reported in Ref. [8]. No irregularities are observed for the resonance widths and intensities of the $^1D_2$ series members; the data for Γ and $q(^3P_2)$ are listed in Table VIII. The reduced width $\Gamma_R = \Gamma_n(n^*)^3$ is found to be fairly constant for all series. We obtain as weighted averages $\Gamma_R(^2PD) = 4.0(2)$ eV, $\Gamma_R(^2F) = 0.74(14)$ eV, $\Gamma_R(^2S) = 0.65(8)$ eV, and $\Gamma_R(^2D) = 0.21(5)$ eV.

The members of the first group of this series, $(^1D_2)6s,4d$, are placed by Tech [9] below the $^3P_2$ threshold. As a consequence, the broad structures become lines and the $4d\ ^2D$ and $4d\ ^2P$ lines are separated. The quantum defect $\mu = 1.282$ for $4d\ ^2D_{3/2}$ is close to the values of the $md\ ^2D$, ^2P resonances with $m \geq 5$, while $\mu = 1.176$ for $4d\ ^2P_{3/2}$ is much smaller. The value of $\mu = 1.170$ for $4d\ ^2F$ is slightly smaller than μ in the autoionization region, and $\mu = 3.084$ for $6s\ ^2D_{3/2}$ is marginally greater. However, $\mu = 1.167$ for the line identified in Ref. [9] as $4d\ ^2S$ is surprisingly large compared with $\mu = 0.87$ for $m \geq 5$. Assuming a value of 0.80 to 0.90 for μ would place this line between 11.98 and 11.89 eV, allowing us to tentatively assign the line to peak 11 in Fig. 5 at 11.968 eV.

In Fig. 9 a comparison is presented for the total cross section σ_{tot} obtained directly in an ion-yield measurement and σ_{tot} obtained as $\Sigma\sigma_i$ shown in Fig. 3 of Ref. [18]. Following subtraction of a suitable background for the raw ion spectrum, the two σ_{tot} spectra are matched at 12.770 eV. Excellent accord is achieved across the entire group, attesting to the reliability of both approaches.

D. The $(^1S_0)ns,md$ series

An overview of this series is given in Fig. 3 as observed in the $(^1D_2)\epsilon\ell$ exit channel. This is a recording of the entire series; only the lowest group of the series had been seen before in an ion-yield experiment [11]. However, the total cross section across the series was calculated more recently [4]. While the two expected series, $(^1S_0)ns$ and $(^1S_0)md$, are clearly delineated in both experiment and theory, the ''background'' cross section displays a slope in the experiment and is flat in theory. The slope is likely to be due to a molecular contribution and a decreasing transmission of the electron analyzers toward low kinetic energies. Both contri-

TABLE VII. Energies and quantum defects μ for the $(^1D_2)md(^2PD,^2S,^2F)$ and $(^1D_2)ns\ ^2D$ series.

m,n	Energy (eV) [a]				μ				ΔE (meV) [b]					
									Ref. [11]			Ref. [8]		
	^2PD	^2S	^2F	^2D	^2PD	^2S	^2F	^2D	^2PD	^2S	^2D	^2PD	^2S	^2D
5,7	12.324	12.521	12.356	12.429	1.291(2)	0.853(3)	1.229(2)	3.076(2)	−5	+6	+5	−27	−50	+4
6,8	12.693	12.796	12.709	12.752	1.315(4)	0.866(5)	1.251(4)	3.073(4)	+2	+3	+2	−4	+3	+1
7,9	12.891	12.951	12.899	12.927	1.328(7)	0.864(8)	1.260(7)	3.063(8)	−2	+2	0	−2	+1	0
8,10	13.008	13.045	13.013	13.029	1.311(11)	0.86(1)	1.264(11)	3.063(12)	−4	+2	+1	−5	+1	+2
9,11	13.082	13.107	13.086	13.097	1.325(17)	0.87(2)	1.259(17)	3.06(2)		−1	−1	−6	0	+1
10,12	13.132	13.149	13.135	13.143	1.33(3)	0.87(3)	1.25(2)	3.07(3)				−4	+1	−1
11,13	13.193	13.179	13.169	13.175	1.34(4)	0.89(4)	1.28(3)	3.06(4)				−27	+1	0
12,14	13.213	13.202	13.194	13.199	1.33(6)	0.90(5)	1.28(4)	3.07(5)				−22	+1	+1
13,15	13.228	13.220	13.214	13.218	1.33(7)	0.89(7)	1.27(6)	3.02(6)				−17	+1	−1
14,16	13.240	13.233	13.229	13.231	1.33(9)	0.90(8)	1.25(8)	3.07(8)				−13		
15	13.249	13.244	13.241		1.32(11)	0.88(10)	1.23(10)					−10		
16	13.257	13.253			1.33(14)	0.89(12)						−5		
17	13.264				1.31(17)							−7		
18	13.269				1.3(2)							−5		
19	13.274				1.3(3)							−4		
20	13.278				1.2(3)									

[a]Uncertainty is ±2 meV.
[b]Referred to our energy E.

butions could be corrected only approximately; for example, several broad molecular humps still appear near 14 eV. In contrast to the $(^1D_2)\epsilon\ell$ channel, the $(^3P_2)\epsilon\ell$ channel (not shown) displays no molecular contamination, as expected from the PES spectra, and a flat background, which would not be subject to transmission effects at the higher energies of these electrons (see Figs. 1 and 2). Energies and quantum defects for series members up to the seventh group are summarized in Table IX. Again $\mu \approx 3.09$ for the s series and $\mu \approx 1.30$ for the d series following the same trend as found in Secs. IV B and IV C for the corresponding series converging to $Br^+\ ^3P_{1,0}$ and $^1D_2$. The third group of the series, with its $8s\ ^2S, 6d\ ^2D$ members, was subject to a detailed investigation in all channels. The results are shown in Fig. 10. Both the σ_i and β_i are based on the same $d\sigma_i/d\Omega$ CIS spectra at 0° and 90°, and the ''fits'' to the β_i and σ_i are derived from the Shore fits of the $d\sigma_i/d\Omega$ spectra. CIS scans of σ_i at the

TABLE VIII. Resonance widths Γ and shape parameters $q(^3P_2)$ for $(^1D_2)ns,md$ series members.[a]

Resonance	Γ (meV)	$q(^3P_2)$
$6d\ ^2PD$	35(2)	1.8(2)
$7d$	22(1)	1.5(1)
$8d$	16(1)	1.4(1)
$9d$	10(1)	1.5(1)
$6d\ ^2F$	5.4(1.1)	0.4(3)
$7d$	5(1)	−0.2(1)
$8d$	3.4(2)	−0.2(1)
$6d\ ^2S$	4.5(5)	6.7(4)
$7d$	2.9(6)	8.7(1)
$8d$	1.9(8)	10.0(5)
$8s\ ^2D$	1.9(6)	4.9(4)
$9s$	1.1(5)	3.9(1)
$10s$	≈0.8	≈2.2

[a]Widths for the $9s,7d$ group and higher are derived from $(^3P_2)\epsilon\ell$ data only.

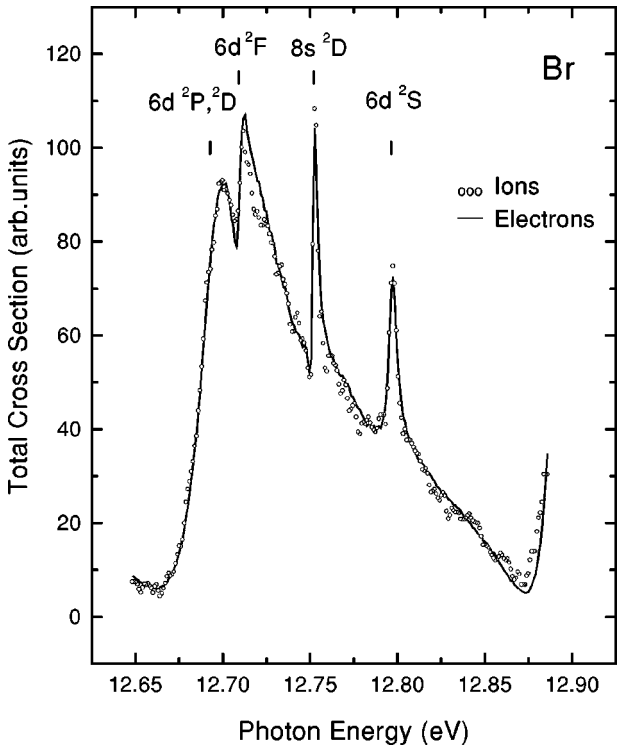

FIG. 9. Relative total cross sections for the $(^1D_2)8s,6d$ group; comparison of the ion-yield data with the electron emission data. The bandpass is 2 meV, and the step size is 1 meV for both spectra.

TABLE IX. Energies and quantum defects μ for the $(^1S)ns,md$ series.

Resonance	Energy (eV) [a]	μ
$4d\ ^2D$	13.485 [b]	1.238(2)
$5d\ ^2D$	14.283	1.284(3)
$6d\ ^2D$	14.653	1.301(6)
$7d\ ^2D$	14.850	1.299(11)
$8d\ ^2D$	14.965	1.312(17)
$9d\ ^2D$	15.040	1.30(3)
$10d\ ^2D$	15.091	1.25(4)
$11d\ ^2D$	15.125	1.28(6)
$6s\ ^2S$	13.657 [c]	3.094(2)
$7s\ ^2S$	14.381	3.084(4)
$8s\ ^2S$	14.707	3.077(7)
$9s\ ^2S$	14.881	3.075(12)
$10s\ ^2S$	14.984	3.088(19)
$11s\ ^2S$	15.052	3.08(3)
$12s\ ^2S$	15.096	3.11(4)
$13s\ ^2S$	15.130	3.10(6)

[a]Uncertainty is ± 2 meV.
[b]Reference [11] reports 13.476 eV.
[c]Reference [11] reports 13.655 eV.

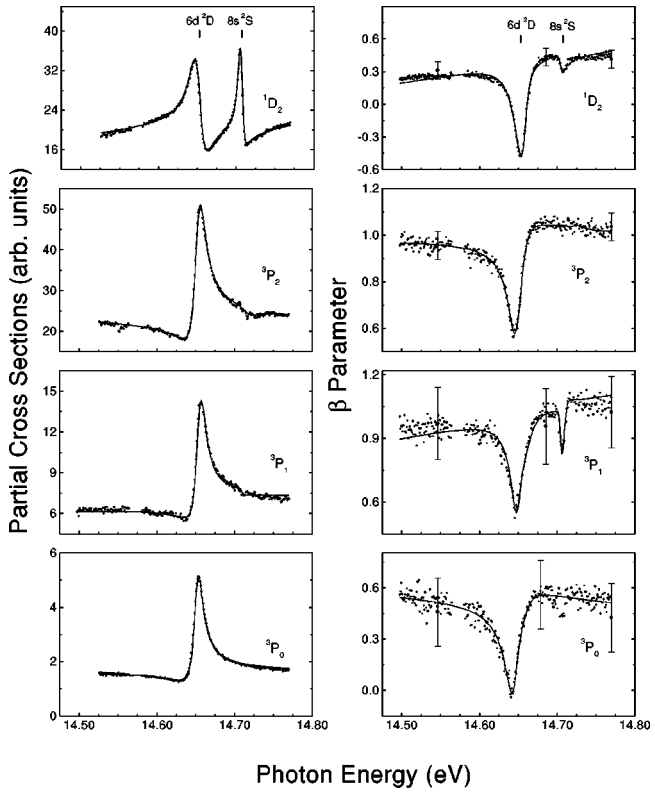

FIG. 10. Partial cross sections σ_i and β_i parameters for the $Br^+(^1D_2)$ and $Br^+(^3P_{2,1,0})$ components across the $(^1S_0)8s,6d$ resonance group. Solid points are data, and all solid lines are calculated from convoluted Shore fits of the differential cross sections at 0° and 90°. Points with error bars are PES data. Scales for σ_i are matched to one another. The bandpass is 4 meV and the step size is 1 meV.

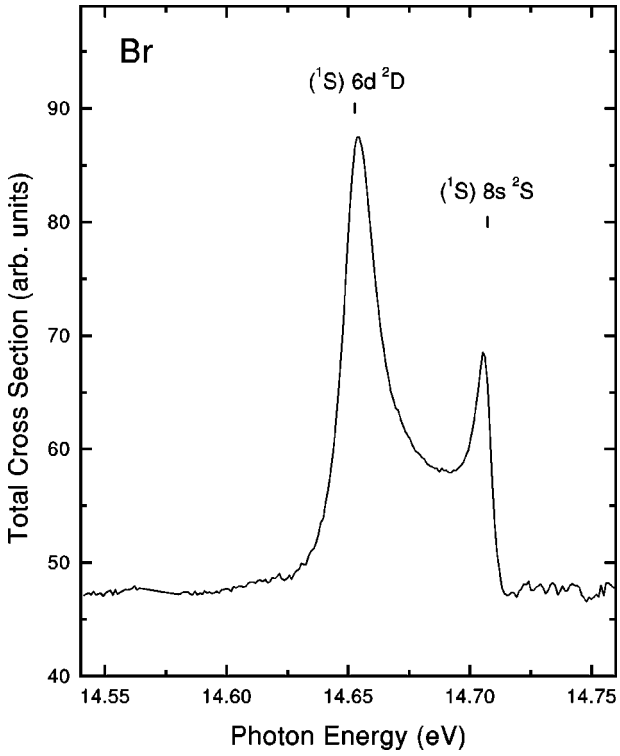

FIG. 11. The relative total cross section of the $(^1S_0)8s,6d$ group. Data are averaged from the sums of σ_i obtained directly at θ_m and indirectly from $d\sigma_i/d\Omega$ at 0° and 90° (see Fig. 10). The bandpass is 4 meV and the step size 1 meV.

angle θ_m are in satisfactory agreement with the indirectly obtained σ_i seen in Fig. 10. The sum of all σ_i, equivalent to $\sigma_{\rm tot}$, is displayed in Fig. 11 as a weighted average of the directly and indirectly obtained σ_i.

The md members are broad, as is usual for d electrons, but the ns members, although narrower than the md members, are relatively wide. Excitations to md are allowed to decay into all channels, $^1D_2, ^3P_2, ^3P_1, ^3P_0$, while excitations to ns should decay only into $^1D_2$. This preferred behavior is indeed observed. However, the $\beta(^3P_1)$ scan over the $8s\ ^2S$ resonance reveals a signal. This would indicate that the $(^1D_2)8s\ ^2S_{1/2}$ would interact with a total final state having the same total angular momentum $j=1/2$. The dip in β_i for $6d\ ^2D$ extends over 0.3–0.6 units, and the value of β_i is lowest in $^1D_2$ and decreases from $^3P_2$ to $^3P_0$. This is probably largely an energy effect because β has a tendency to rise from a low value somewhat above threshold to higher values with increasing energy of the ejected electron. Returning to σ_i, it is to be noted that the shape parameter q_i changes sign between the $(^1D_2)\epsilon\ell$ and $(^3P_J)\epsilon\ell$ channels. However, the shapes for the ^3P_J-fine-structure profiles are nearly the same as seen in Fig. 10 and in Table X where the results of a detailed analysis of the $8s,6d$ group are tabulated. Values for q_i are summarized in Table XI along with the resonance width values for several of the broader members. From the entries in Table XI, the reduced widths are derived: the weighted average values are $\Gamma_R(^2D)=1.9(3)$ eV and $\Gamma_R(^2S)=0.8(1)$ eV. These fairly constant values for Γ_R, and the constant values for μ and q demonstrate that the ^1S based series are not perturbed.

TABLE X. Shape parameters q_i for the $(^1S_0)8s,6d$ group.

Br^+	$6d\ ^2D$	$8s\ ^2S$
$^1D_2$	−1.3(2)	−2.4(3)
$^3P_2$	2.4(2)	
$^3P_1$	2.7(1)	
$^3P_0$	3.1(1)	
Total	4.8(2)	−2.2(1)

V. CONCLUSIONS

Autoionizing resonances of all series converging to the $Br^+\ ^3P_{1,0}$, $^1D_2$, and $^1S_0$ ionization thresholds have been studied at the fine detail that is afforded by electron spectrometry in tandem with a synchrotron radiation source. This study offers a comprehensive view of the spectroscopic and dynamic properties of the resonance series involving the excitation of a $4p$ electron, $4p\rightarrow ns,md$, and the ionization into the final (ionic) continuum channels which are energetically allowed. The resolution achieved in this work exceeds that used in previous spectroscopic work, as do the signal strength and the signal-to-noise ratio. As a result, new series members could be identified in all series, and the $^1S_0$-based series could be fully delineated. Quantum defects were found to be constant, or nearly constant, for all series with $\mu \approx 1.3$ for d electrons and $\mu \approx 3.1$ for s electrons regardless of the ionization limit. This demonstrates that the orbital momentum determines the behavior of the Rydberg series also in an open-shell configuration, and the Br^+ $4p^4(^3P_{1,0},^1D_2,^1S_0)$ states may be regarded as ''core'' states exerting only a minor *core-specific* influence on the behavior of the series. An exception occurs for the LS-forbidden $(^1D)md\ ^2S$ resonance series which has a lower μ value of about 0.9. In this case, core participation is required for autoionization to take place.

Partial cross sections σ_i and electron angular distribution parameters β_i have been presented for selected groups of each major series. From these data additional dynamic properties such as shape parameters and resonance widths have been extracted. The cross section results, which were supplemented by a determination of the total cross section by way of a total ion-yield measurement, allowed us also to determine the proper resonance energies by a fitting procedure of the resonance profiles. In all instances, except for the LS-forbidden $(^1D)md\ ^2S,^2F$ series, the d resonances were seen to be broad and the s resonances to be narrow, both observations being in accord with expectations. The general behavior of σ_i and β_i for the $^1D_2$-based series resembles that observed in Cl, and in fact that of the neighboring closed-shell atom Kr. However, the open-shell character of Br, and Cl, introduces greater complexity and facilitates spin-orbit interactions. Resonance widths and intensities behave in a regular fashion for the $^1D_2$- and $^1S_0$-based series and are indicative, together with the quantum defect, that these series are not exposed to a perturber. By contrast, the intensities of the members of the $^3P_{1,0}$-based series are very irregular. This can be attributed to the influence of the lowest $(^1D_2)ns,md$ members and to other possible interseries interactions. Our results for the energies and quantum defects agree satisfactorily with earlier data where available. However, variances are observed for the total cross sections of the $^3P_{1,0}$ series, and the spin-orbit-induced $(^1D_2)md\ ^2F$ series appears only in our experimental data. The only theoretical calculation, the eigenchannel R-matrix approach with a multichannel quantum defect extension presented by Robicheaux and Greene, is in good accord throughout with our (relative) total cross section measurements. However, a comparison with theory of our detailed data pertaining to partial cross sections and β parameters, as well as resonance widths and shape parameters, will have to await an explicit calculation of these dynamic parameters at an equally differentiated level.

Finally, we note that this work on the $4p\rightarrow ns,md$ excitations and an earlier study [17] of the $4s\rightarrow np$ excitations provide us with a virtually complete account of the electronic structure and dynamics in the autoionization regimes for the bromine atom. Similar, but somewhat less comprehensive results for the chlorine atom in the corresponding autoionization regimes [32,35] complement these results for bromine.

TABLE XI. Resonance widths Γ and shape parameters q_i for $(^1S_0)ns,md$ series members.

Member	Γ (meV)	$q(^1D_2)$	$q(^3P_2)$
$5d\ ^2D$	31(3)	−1.3(2)	2.7(2)
$6d\ ^2D$	15(2)	−1.3(2)	2.4(2)
$7d\ ^2D$	11(1)	−1.2(2)	2.4(2)
$8d\ ^2D$	9(1)	−1.2(2)	2.3(2)
$7s\ ^2S$	10(3)	−3.2(3)	
$8s\ ^2S$	7(1)	−2.4(3)	
$9s\ ^2S$	5(2)	−2.2(3)	
$10s\ ^2S$	3(1)	−2.2(3)	

ACKNOWLEDGMENTS

This work was supported by NSF Grant No. PHY-9507573. The loan of equipment by the Oak Ridge National Laboratory is gratefully acknowledged. The SRC is supported under NSF Grant No. DMR-9531009.

[1] S. T. Manson, A. Msezane, A. F. Starace, and S. Shahabi, Phys. Rev. A **20**, 1005 (1979).

[2] J. Berkowitz and G. L. Goodman, J. Chem. Phys. **71**, 1754 (1979).

[3] J. Schirmer, L. S. Cederbaum, and J. Kiessling, Phys. Rev. A **22**, 2696 (1980).

[4] F. Robicheaux and C. H. Greene, Phys. Rev. A **46**, 3821 (1992).

[5] F. Robicheaux and C. H. Greene, Phys. Rev. A **47**, 1066 (1993).

[6] C. E. Moore, *Atomic Energy Levels*, Natl. Bur. Stand. (U.S.) Ref. Data Ser. No. 35 (U.S. GPO, Washington, DC, 1971).

[7] R. E. Huffman, J. C. Larrabee, and Y. Tanaka, J. Chem. Phys. **47**, 856 (1967).
[8] V. N. Sarma and Y. N. Joshi, J. Phys. B **16**, 1671 (1983).
[9] J. L. Tech, J. Res. Natl. Bur. Stand. **67A**, 505 (1963).
[10] W. C. Martin and J. L. Tech, J. Opt. Soc. Am. **51**, 591 (1961).
[11] B. Ruščić, J. P. Greene, and J. Berkowitz, J. Phys. B **17**, 1503 (1984).
[12] D. M. de Leeuw, R. Mooyman, and C. A. de Lange, Chem. Phys. Lett. **54**, 231 (1978).
[13] K. Kimura, T. Yamasaki, and Y. Achiba, Chem. Phys. Lett. **58**, 104 (1978).
[14] W. J. van der Meer, P. van der Meulen, and C. A. de Lange, Chem. Phys. **115**, 109 (1987).
[15] J. B. Peel and E. I. von Nagy-Felsobuki, Spectrochim. Acta B **43**, 217 (1988).
[16] B. G. Koenders, K. E. Drabe, and C. A. de Lange, Chem. Phys. Lett. **138**, 1 (1987).
[17] P. van der Meulen, M. O. Krause, and C. A. de Lange, J. Phys. B **25**, 97 (1992).
[18] S. Benzaid, A. Menzel, J. Jiménez-Mier, S. J. Schaphorst, M. O. Krause, and C. D. Caldwell, Phys. Rev. A **54**, R2537 (1996).
[19] C. D. Caldwell and M. O. Krause, in *Handbook of Atomic, Molecular, and Optical Physics*, edited by G. W. F. Drake (AIP Press, New York, 1996), Chap. 59.
[20] B. W. Shore, J. Opt. Soc. Am. **57**, 881 (1967).
[21] B. W. Shore, Phys. Rev. **171**, 43 (1968).
[22] J. Z. Wu, S. B. Whitfield, C. D. Caldwell, M. O. Krause, P. van der Meulen, and A. Fahlman, Phys. Rev. A **42**, 1350 (1990).
[23] U. Fano, Phys. Rev. **124**, 1866 (1961).
[24] S. B. Whitfield, M. O. Krause, P. van der Meulen, and C. D. Caldwell, Phys. Rev. A **50**, 1269 (1994).
[25] M. O. Krause, T. A. Carlson, and A. Fahlman, Phys. Rev. A **30**, 1316 (1984).
[26] M. O. Krause and C. D. Caldwell, in *VUV and Soft X-Ray Photoionization*, edited by U. Becker and D. A. Shirley (Plenum Press, New York, 1996), Chap. 6.
[27] A. Menzel, S. P. Frigo, S. B. Whitfield, C. D. Caldwell, and M. O. Krause, Phys. Rev. A **54**, 2080 (1996).
[28] K. Yoshino and D. D. Freeman, J. Opt. Soc. Am. B **2**, 1268 (1985).
[29] K. Yoshino and Y. Tanaka, J. Opt. Soc. Am. **69**, 159 (1979).
[30] J. Berkowitz, Adv. Chem. Phys. **72**, 1 (1988).
[31] W. R. Johnson, K. T. Cheng, K. N. Huang, and M. Le Dourneuf, Phys. Rev. A **22**, 989 (1980).
[32] J. Jiménez-Mier, S. J. Schaphorst, C. D. Caldwell, and M. O. Krause, Phys. Rev. A **56**, 3659 (1997).
[33] N. M. Kabachnik and I. P. Sazhina, J. Phys. B **17**, 1335 (1984).
[34] We agree with B. Ruščić *et al.*, Ref. [11], on the reassignment of the series in Table 21 of Ref. [8] to $md\ ^2S$.
[35] P. van der Meulen, M. O. Krause, C. D. Caldwell, S. B. Whitfield, and C. A. de Lange, J. Phys. B **24**, L573 (1991); Phys. Rev. A **46**, 2468 (1992).